Lawrence Berkeley National Laboratory

Title
Ferritic stainless steel interconnects for protonic ceramic electrochemical cell stacks: Oxidation behavior and protective coatings

Authors
Wang, Ruofan
Sun, Zhihao
Choi, Jung-Pyung
et al.

Ferritic Stainless Steel Interconnects for Protonic Ceramic Electrochemical Cell Stacks: Oxidation Behavior and Protective Coatings

Ruofan Wang[1], Zhihao Sun[2], Jung-Pyung Choi[3], Soumendra N. Basu[2], Jeffry W. Stevenson[3], Michael C. Tucker[1,*]

[1] Energy Storage and Distributed Resources Division, Lawrence Berkeley National Laboratory, Berkeley, California 94720, USA

[2] Division of Materials Science and Engineering, Boston University, Brookline, Massachusetts 02446, USA

[3] Pacific Northwest National Laboratory, Richland, Washington 99352, USA

*Corresponding author:

Michael C. Tucker, mctucker@lbl.gov, Tel +1 (510) 486-5304, Mail stop 62-203, 1 Cyclotron Road, Berkeley, CA 94720, United States

Abstract

Protonic ceramic fuel or electrolysis cells (PCFC/PCEC) have shown promising performance at intermediate temperatures. However, these technologies have not yet been demonstrated in a stack, hence the oxidation behavior of the metallic interconnect under relevant operating environments is unknown. In this work, ferritic stainless steels 430 SS, 441 SS, and Crofer 22 APU were investigated for their use as interconnect materials in the PCFC/PCEC stack. The bare metal sheets were exposed to a humidified air environment in the temperature range from 450 °C to 650 °C, to simulate their application in a PCFC cathode or PCEC anode. Breakaway oxidation with rapid weight gain and Fe outward diffusion/oxidation was observed on all the selected

stainless steel materials. A protective coating is deemed necessary to prevent the metallic interconnect from oxidizing.

To mitigate the observed breakaway oxidation, state-of-the-art protective coatings, Y_2O_3, $Ce_{0.02}Mn_{1.49}Co_{1.49}O_4$, $CuMn_{1.8}O_4$ and Ce/Co, were applied to the stainless steel sheets and their oxidation resistance was investigated. Dual atmosphere testing further validated the effectiveness of the protective coatings in realistic PCFC/PCEC environments, with a hydrogen gradient across the interconnect. Several combinations of metal and coating material were found to be viable for use as the interconnect for PCFC/PCEC stacks.

Keywords: Protonic ceramic fuel cell; Protonic ceramic electrolysis cell; Interconnect oxidation; Protective coatings; Dual atmosphere; Oxidation

1. Introduction

Protonic ceramic electrochemical cells (PCEC) that incorporate proton-conducting oxides as electrolyte materials have attracted increasing research attention in recent years. Compared with the oxide-ion conducting electrolytes used in conventional solid oxide fuel/electrolysis cells, proton-conducting oxides possess higher ionic conductivity at an intermediate temperature range (400–600 °C), therefore enabling higher performance of protonic ceramic fuel and electrolysis cells (PCFCs/PCECs) in this temperature range [1-6].
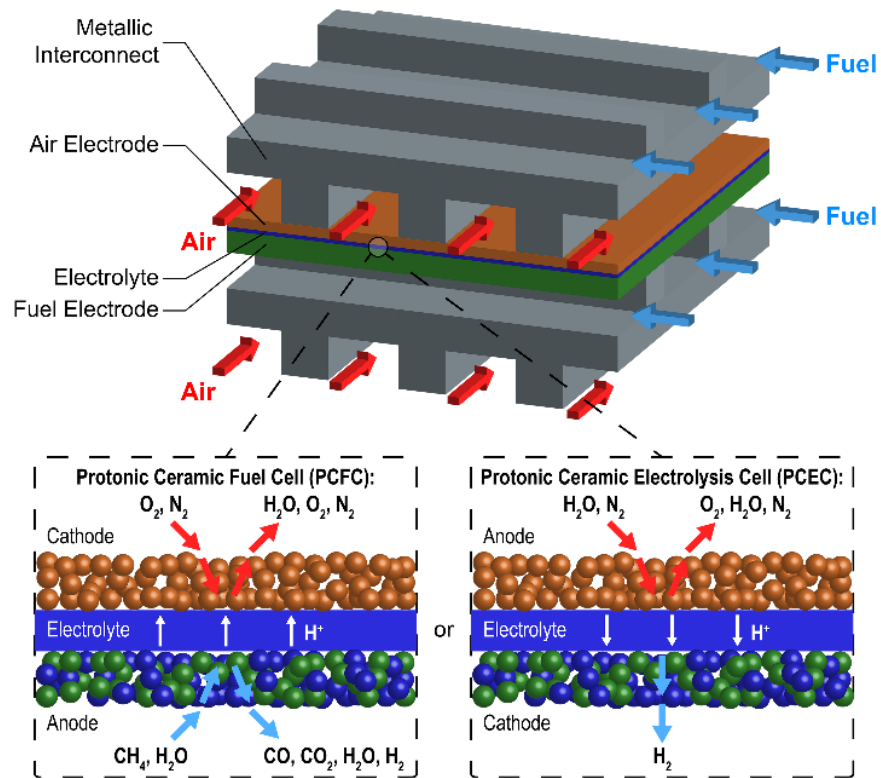
Protonic ceramic cells offer many other advantages. Compared to conventional solid oxide fuel cells (SOFC), protonic ceramic fuel cells have higher methane conversion [1, 7] and higher carbon coking and sulfur-poisoning resistance [8]. Protonic ceramic cells also can be operated as

2

electrolyzers for high temperature water splitting and for co-electrolysis of CO_2 and H_2O [9-12]. To split water, steam is supplied to the oxygen electrode of the PCEC and dry hydrogen is produced in the fuel electrode, so removal of steam from hydrogen is not needed, and electrochemical compression of H_2 can be achieved [4, 5]. For co-electrolysis of CO_2 and H_2O, the lower operating temperature of PCECs favors in-situ Fischer–Tropsch reactions [13], which are the rate-controlling reactions for co-electrolysis in solid oxide electrolyzer cells (SOEC) [14]. The lower operating temperature further allows the use of less expensive interconnect and balance-of-plant (BoP) materials, resulting in lower manufacturing costs [15].

Although protonic ceramic cell technology has shown great promise, most of the research and development efforts have focused only on the single cell level [1, 2, 4, 7, 16-19]. Recently, researchers from South Korea demonstrated a scaled-up (5×5 cm^2) single protonic ceramic fuel cell that showed exciting high initial performance at intermediate temperatures [20]. Up to now, however, stack development of protonic ceramic cells has not been reported. Much work is still needed to realize large-scale application of protonic ceramic cell stacks.

To implement protonic ceramic cells at a stack/system scale, it is important to select interconnect materials that are compatible with PCFC/PCEC operating atmospheres and temperatures. For PCFC, one side of the interconnect is exposed to a fuel-water mixture (water is needed for internal reforming), and the other side is exposed to air and generates humidity (humidity is present because protons react with oxygen molecules in air), as shown schematically in Fig 1. When a protonic ceramic cell is used for steam electrolysis, steam is supplied to the air electrode, with oxygen produced on the same side, while dry hydrogen is generated at the fuel electrode. It

is important to realize that the working environment of a PCFC/PCEC interconnect is very different from that of a SOFC/SOEC interconnect. In both PCFC and PCEC cases, one side of the interconnect is exposed to high steam content in an oxidizing environment (especially in the case of electrolysis), which may result in rapid degradation of the interconnect at intermediate temperatures.

Figure 1. Schematic of protonic ceramic fuel cell (PCFC) and protonic ceramic electrolysis cell (PCEC) operation in the stack.

For conventional SOFC/SOEC stacks, the interconnect and its coating materials have been extensively developed [21-31]. At present, ferritic stainless steel alloys are the most popular choice for intermediate temperature (approximately 600 to 800 °C) SOFC interconnects or

substrates, due to low manufacturing cost, suitable oxidation rate, close thermal expansion match with SOFC components, and high electrical and thermal conductivity [28, 32-36]. For PCFC/PCEC, the choice of metallic interconnect is further supported because ceramic interconnect materials do not have comparable electrical conductivity at relatively lower operating temperature. Very few investigations of metallic interconnect materials under PCFC/PCEC operating conditions have been reported. Skilbred et al. reported that Sandvik Sanergy HT (a ferritic stainless steel that is not the same composition as the newer Sandvik Sanergy HT 441 used in this work) is a potential interconnect material for a LaNbO$_4$-based PCFC [37, 38]. However, the study focused on relatively high temperature, 700 to 1000°C. Alnegren et al. investigated the dual atmosphere effect on corrosion behavior of stainless steel 441 at 600 °C [39-41]. So far, no oxidation study has evaluated a PCFC/PCEC interconnect in both an intermediate temperature range and a higher humidity oxidizing environment. Furthermore, oxidation-resistant interconnect coatings have not yet been explored under relevant PCFC/PCEC conditions.

In this study, the feasibility of using existing SOFC metallic interconnect materials in PCFC/PCEC applications is evaluated. Stainless-steel sheets, type 430, 441, and Crofer 22 APU, are exposed to relevant PCFC/PCEC operating conditions (mainly in humidified air) and the oxidation behavior is analyzed. In addition to bare alloys, state-of-the-art protective coatings, reactive element oxide coating Y$_2$O$_3$, spinel oxide coatings Ce$_{0.05}$Mn$_{1.475}$Co$_{1.475}$O$_4$ (Ce-MC) and CuMn$_{1.8}$O$_4$ (CuMn), and metallic conversion coating Ce/Co, were applied on the metallic interconnect, and the effectiveness of the coatings for reducing the oxidation rate is determined. A dual atmosphere oxidation study using humidified air and dry hydrogen on opposite sides of

the metal further validates the effectiveness of the protective coatings in PCFC/PCEC environments with a hydrogen gradient. The objectives of this study are (1) to illustrate the oxidation behavior of ferritic stainless steels in PCFC/PCEC environments, and (2) to identify material sets from previous SOFC research that are viable for PCFC/PCEC stack development.

2. Experimental

2.1. Assessment of oxidation resistance

Stainless steel sheets, 430 SS (McMaster, USA), 441 SS (Alleghany Ludlum, USA), and Crofer 22 APU (Nexceris, USA) were obtained commercially. These materials were selected because (a) their coefficients of thermal expansion (CTE) are all near 12×10^{-6}/K, close to that of the commonly used PCFC electrolyte and electrode materials (such as BZCY); and (b) they are commonly used as SOFC interconnect materials, thus available knowledge can be transferred to PCFC/PCEC applications. Table 1 summarizes the composition of the selected stainless steels.

	Fe	Cr	C	Mn	Si	S	P	Ti	Ni	Nb	La	Cu	Al
430 SS	bal.	16-18	0.12 (max)	1 (max)	1 (max)	0.03 (max)	0.04 (max)	-	0.5 (max)	-	-	-	-
441 SS	bal.	17.5-18.5	0.03 (max)	1 (max)	1 (max)	0.015 (max)	0.04 (max)	0.1-0.6	-	1 (max)	-	-	-
Crofer 22 APU	bal.	22-24	0.03 (max)	0.3-0.8	0.5 (max)	0.02 (max)	0.05 (max)	0.03-0.2	-	-	0.2 (max)	0.5 (max)	0.5 (max)

Table 1. Composition (wt%) of stainless steels investigated in this study.

The metal sheets were about 0.15 mm thick as received. The sheets were cut into 1.5×1.5 cm^2 coupons and rinsed with acetone and ethanol before oxidation experiments. Oxidation behavior

of the specimens was evaluated at various PCFC/PCEC operating temperatures (450, 550, and 650 °C) by placing the specimens in an alumina sample holder in a tube furnace. A thermocouple was placed next to the samples, and the temperature of the samples deviated less than 5 °C from the target temperature. Weight gain of the samples was measured intermittently for up to 500 hours. At least two identical samples were used for each condition to ensure repeatable results and weight gain values were averaged. A Mettler Toledo XP205 analytical balance (with precision of 0.01 mg) was used for weight gain measurements. Ramping rates for furnace heating and cooling were set at 5 °C/min. Samples were oxidized in humidified air to simulate the PCFC cathode/PCFC anode environment. The absolute humidity was controlled by bubbling air through a distilled water tank with the tank temperature maintained at the required dew point. A Teflon tube downstream of the water bubbler was heated above 100 °C by heating tape to avoid undesired condensation. For comparison, some samples were also exposed to ambient air (Air-~1.5%H_2O), humidified H_2 (2.8%H_2-Ar-50%H_2O), and dry H_2 (2.8%H_2-Ar), which simulated atmospheres found in an SOFC cathode, an SOFC anode, and a PCFC anode, respectively.

2.2. Coating materials and procedure

State-of-the-art coating materials were also applied to the alloy surfaces to evaluate their oxidation resistance. These included: (a) Y_2O_3, (b) $Ce_{0.02}Mn_{1.49}Co_{1.49}O_4$ spinel (Ce-MC), and (c) $CuMn_{1.8}O_4$ spinel (CuMn). A sol-gel dip coating was used to prepare the Y_2O_3 coating [42-46]. $Y(NO_3)_3 \cdot 6H_2O$ (Sigma-Aldrich, 99.8%) was mixed with citric acid monohydrate (as a chelating agent) in ethylene glycol to make a sol-gel solution with a Y concentration of 4 M. The solution was stirred on a hot plate at 80 °C for 24 h, after which the precursor solution was formed. The dip coating was performed with a customized dip coater with a dip speed of 10 cm/min. After the

substrates were submerged in the solution for 1 min, the samples were withdrawn and dried in an oven at 80 °C for 3 h. The coating process was completed by annealing the samples in a muffle furnace at 650 °C for 3 h.

The Ce-MC coating was applied by ultrasonic aerosol spraying. The spinel oxide powder was synthesized via the glycine-nitrate combustion process. After the spinel powder was obtained, it was attrition-milled and mixed with a binder system to form a slurry. After applying the slurry on both sides of the metal substrate by spraying, the coated specimens were dried in an oven and then heat-treated in hydrogen at 850 °C for 5 h and then annealed in ambient air at 1000 °C for 1 h. Details of the Ce-MC coating process can be found elsewhere [47-49].

The CuMn coating was produced by electrophoretic deposition (EPD). The spinel oxide powder was produced via the glycine-nitrate combustion process. The synthesized powder was calcined and ball-milled, and then mixed with ethanol, acetone, and iodine to form a suspension for EPD. EPD was performed with a constant voltage of 20 V for 10 min, with 1.5 cm separation between the electrodes. After EPD was completed, the samples were heat-treated in a reducing environment (2% H_2 - Ar) for 12 h at 1000 °C and then annealed in ambient air at 750 °C for 100 h. Details of the $CuMn_{1.8}O_4$ spinel coating preparation can be found elsewhere [28, 50].

Sanergy® HT 441 (Sandvik Materials Technology), which is 441 steel with a 10 nm Ce/ 640 nm Co coating prepared via physical vapor deposition (PVD), was also investigated [51, 52]. Prior to the oxidation study, the Ce/Co coated Sanergy HT 441 was pre-oxidized at 900 °C for 10 min to convert metallic Co into Co_3O_4.

Table 2 lists the coating materials and methods, and compares their coefficients of thermal expansion (CTE) to the substrate materials.

Coating Material	Coating Method	CTE (20-800 ℃)	Stainless Steel	CTE (20-800 ℃)
Y_2O_3	Sol-gel dip coating	8.1×10^{-6}/K	430 SS	11.9×10^{-6}/K
$Ce_{0.02}Mn_{1.49}Co_{1.49}O_4$	Aerosol spraying	11.5×10^{-6}/K	441 SS	12.4×10^{-6}/K
$CuMn_{1.8}O_4$	Electrophoretic deposition	12.2×10^{-6}/K	Crofer 22 APU	11.9×10^{-6}/K
Co_3O_4 [a]	Physical vapor deposition	9.3×10^{-6}/K		

[a] For the Ce/Co coating, the CTE of Co_3O_4 is listed because Co_3O_4 is the major coating material after converting metallic Co [52].

Table 2. Coefficient of thermal expansions of stainless steels and coating materials investigated in this study.

2.3. Dual atmosphere testing

Selected combinations of substrate and coating were also subjected to dual atmosphere oxidation to simulate the realistic operating condition of a metallic interconnect in PCFC/PCEC stacks. The schematic of the dual atmosphere exposure setup is shown in Fig. S1. Metal coupons were fixed on top of a metal tube with a glass seal (GM31107, Schott). On one side of the sample, 50% humidified air was circulated to simulate the environment in PCFC cathode or PCEC anode channels. The other side of the sample was exposed to 2.8%H_2-Ar mixture to simulate a dry H_2

environment in the PCFC anode or PCEC cathode channels. Flow rates of both air and 2.8%H_2-Ar were maintained at 200 ml/min. The specimen was exposed at 650 °C for 500 h without interruption, and the leak tightness was checked every 24 h to ensure there was no cross-leak through the glass seal. After dual atmosphere exposure, the microstructure of the samples was examined.

2.4. Materials Characterization

For bare alloys, the oxide scale phases formed after exposure to humidified air were examined by XRD using a Bruker D2 PHASER X-ray diffractometer with CuKα radiation. After the single or dual atmosphere oxidation was completed, cross sections of the samples were mounted in epoxy and polished down to 0.05 μm. The microstructure of the oxide scales and coatings were observed with scanning electron microscopy (SEM, JEOL-7500F) and energy dispersive X-ray spectroscopy (EDS, Thermo Scientific).

3. Results and Discussion

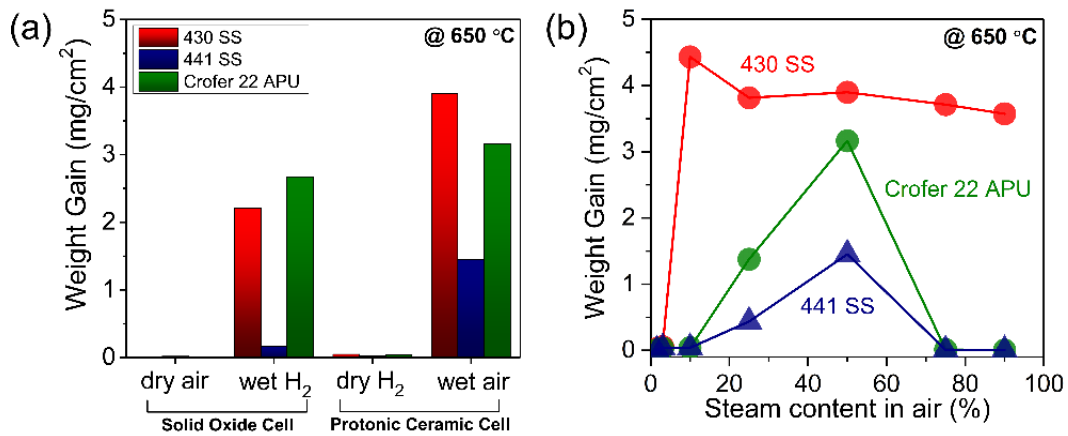### 3.1. Oxidation behavior of uncoated stainless steels

The uncoated stainless steels (430 SS, 441 SS, and Crofer 22 APU) were first exposed to different SOFC/SOEC and PCFC/PCEC conditions at 650 °C for 100 h to identify the environment of interest, that which imposes the most severe oxidation. The temperature 650 °C was selected because it is within the temperature range for operation of both oxygen and proton conductors, and is at the upper end of the range expected for PCFC/PCEC. Four atmospheres were used: (1) ambient air, which simulates the SOFC cathode or SOEC anode environment; (2) 2.8%H_2-Ar-50%H_2O, which simulates the SOFC anode under very high fuel utilization or the

SOEC cathode with high steam input; (3) 2.8% H_2-Ar, which simulates the PCFC anode or PCEC cathode environment; and (4) 50% air-50% H_2O, which simulates the PCFC cathode with high performance or the PCEC anode environment with high steam input. In contrast to SOFC/SOEC experience, where high fuel humidity is the primary concern, we found that for PCFC/PCEC, high oxygen-side humidity is the primary concern, Fig. 2a. The rapid oxidation is referred to as "breakaway oxidation," which is typically caused by formation of Fe-rich oxide scales under conditions where the rate of oxidation exceeds the rate of Cr diffusion from the bulk of the alloy to the surface [53-56]. Note that for normal oxidation resulting in a continuous chromia scale, the oxidation rate is much lower and typically follows parabolic growth rate kinetics, governed by the rates of oxygen uptake and diffusion through the continuously-increasing chromia scale thickness [57-59]. Under these conditions, acceptable weight gain at the end of life is approximately 1.57 mg cm^{-2}, corresponding to 3 μm thickness, as discussed further in Section 3.2. The results clearly showed that at 650 °C, the PCFC cathode/PCEC anode environment could potentially cause more severe breakaway oxidation than the well-studied SOFC anode/SOEC cathode environment. Since the oxidation of stainless steels under SOFC/SOEC conditions have been studied extensively [60-63], the present study focuses on PCFC/PCEC conditions.

3.1.1. Effect of steam content

To determine the steam content that most accelerates oxidation, weight gain after 100h was measured as a function of steam content in air at 650 °C, Fig. 2b. It was found that breakaway oxidation of 430 SS starts at (or lower than) 10% humidity, and weight gain decreases slightly with increasing steam content. In contrast to 430 SS, the weight gain of 441 SS and Crofer 22

APU gradually increased with higher steam content and reach their maximum values at ~ 50% steam content. Interestingly, at 75% and 90% steam content, both 441 SS and Crofer 22 APU did not show significant weight gains, presumably due to lower oxygen partial pressure in the high-steam atmosphere. Note that 441 SS shows the lowest weight gains at all humidity levels compared to the other stainless steels. For the majority of this work, a 50% steam/50% air atmosphere was therefore used because it can evidently promote breakaway oxidation of all three types of stainless steels.

Figure 2. Impact of atmosphere. (a) Area-specific weight gain of uncoated alloys after exposure for 100 h at 650 °C in different fuel cell/electrolysis operating environments: ambient air, 2.8%H_2-Ar-50%H_2O, 2.8%H_2-Ar, and 50%air-50%H_2O. (b) Area-specific weight gain of uncoated alloys as a function of steam content in air after exposure at 650 °C for 100 h.

3.1.2. Effect of temperature

There is a pronounced effect of operating temperature on oxidation behavior at 650, 550, and 450 °C, Fig. 3. For 430 SS, breakaway oxidation occurred at 650 °C within the first 25 h, followed by slower oxidation starting from 100 h, resulting in total weight gain of 4 mg/cm^2 after

500 h. Similar breakaway oxidation also occurred at 550 °C, but less rapidly than at 650 °C. At 450 °C, the oxidation rate was significantly reduced, showing a smooth increase of weight gain to 0.67 mg/cm^2 at 500 h. For 441 SS, the behavior was similar to that of 430 SS at 650 °C, displaying rapid breakaway oxidation within the first 25 h, but with smaller final weight gain (1.5 mg/cm^2) at 500 h compared to 430 SS. At 450 °C, the oxidation of 441 SS was negligible during the 500 h exposure.

For Crofer 22 APU, breakaway oxidation at 650 °C was delayed relative to 430 and 441, and reached a final weight gain of 3.4 mg/cm^2 at 500 h. Similar to 441 SS, Crofer 22 APU did not oxidize significantly within 500 h at 450 °C.
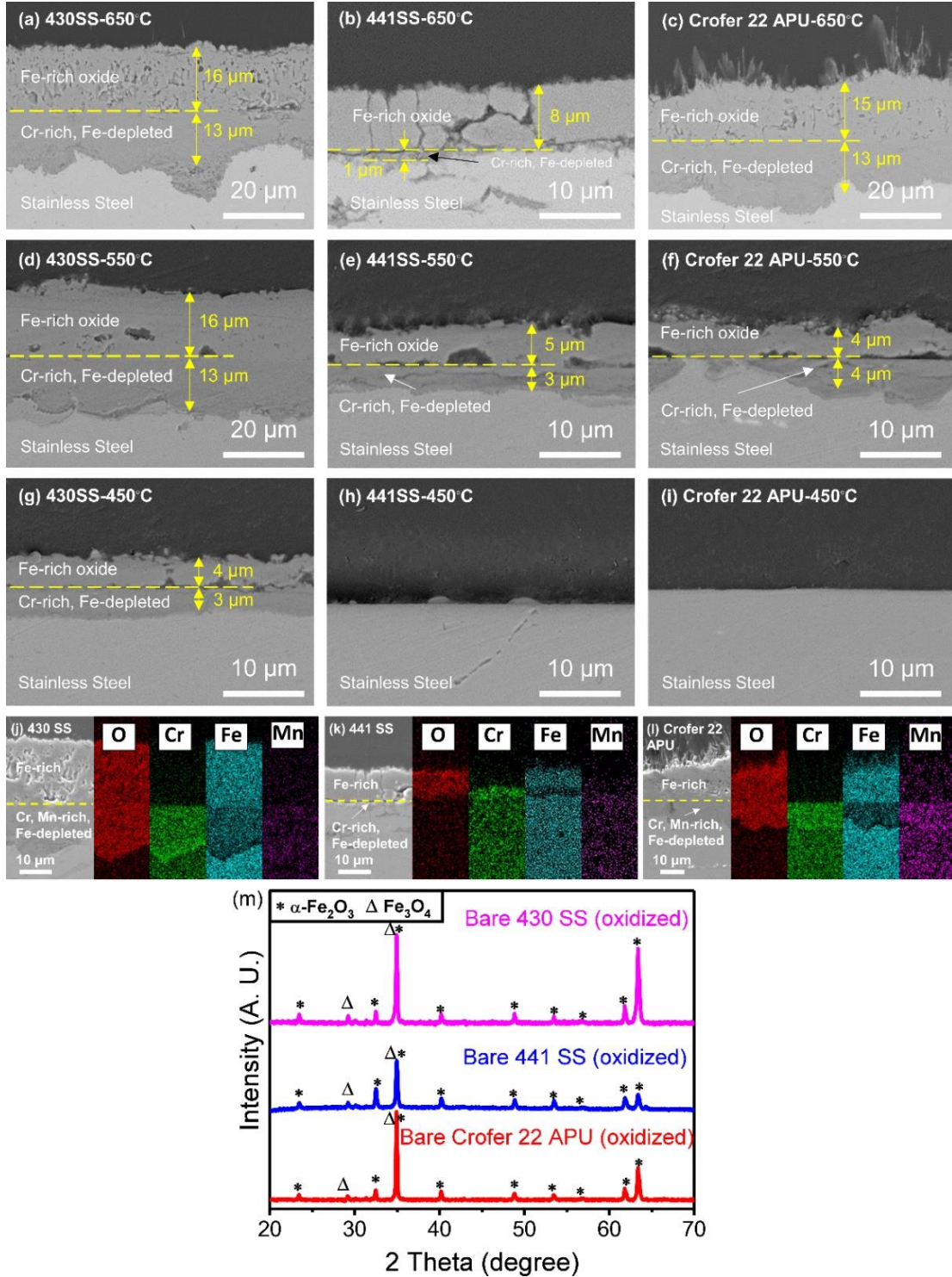

Figure 3. Impact of temperature. Area-specific weight gain of uncoated (a) 430 SS, (b) 441 SS, and (c) Crofer 22 APU, as a function of time in 50% humidified air at 450, 550, and 650 °C.

The microstructures of the oxide layers that formed on the bare alloys after exposure were in good agreement with the weight gain data. After the oxidation test, breakaway oxidation was confirmed by examining specimen cross sections with SEM and EDS, and surfaces with XRD, Fig. 4. For those samples that displayed high weight gain (Fig 3), an outer scale mainly comprised of Fe and O, and an inner oxide scale with Fe depletion and Cr and Mn enrichment

are observed. For 430 SS, significant oxidation occurred at all temperatures (Fig. 4a, d, g). The thicknesses of the oxide scales are approximately 16 and 13 μm, respectively at both 650 and 550 °C, consistent with the similar final weight gains observed at these temperatures. The scales are significantly thinner, 4 and 3 μm, at 450 °C. For 441 SS, significant breakaway oxidation only occurred at 650 and 550 °C, and appears to be barely initiated at 450 °C (Fig. 4b, e, h). The thicknesses of the outer and inner scale layers are approximately 8 and 1 μm at 650 °C, and 5 and 3 μm at 550 °C. For Crofer 22 APU, breakaway oxidation was evident at 650 and 550 °C, but was not observed at 450 °C (Fig. 4c, f, i). The thicknesses of the oxide scales are 15 and 13 μm at 650 °C, and reduced significantly to 4 and 4 μm at 550 °C. For all metals, XRD confirms the formation of α-Fe_2O_3 (hematite) in the outer scale and a cubic spinel structure which is likely (Cr, Mn, Fe)$_3O_4$ in the inner scale, as seen in Fig. 4m.

In summary, it was demonstrated that bare 430 SS, 441 SS, and Crofer 22 APU all experienced breakaway oxidation at 650 °C and 550 °C in a 50% humidified air condition. Fe was observed to be depleted below the alloy surface, and converted to Fe_2O_3 as an outer scale, with (Cr, Mn, Fe)$_3O_4$ formation as an inner scale (due to outward Cr diffusion and inward O diffusion). At 450 °C, breakaway oxidation still occurred on 430 SS, but was not prominent on 441 SS and Crofer 22 APU. This result suggests that bare 441 SS and Crofer 22 APU could be used directly as interconnect materials for a PCFC/PCEC stack if the operating temperature were sufficiently low. At 450 °C, however, the state-of-the-art performance of PCFC/PCEC is not yet high enough to be attractive for commercialization. Based on these results, it is not feasible to use bare ferritic stainless steels as a PCFC/PCEC interconnect, and a protective surface modification or protective coating is necessary.
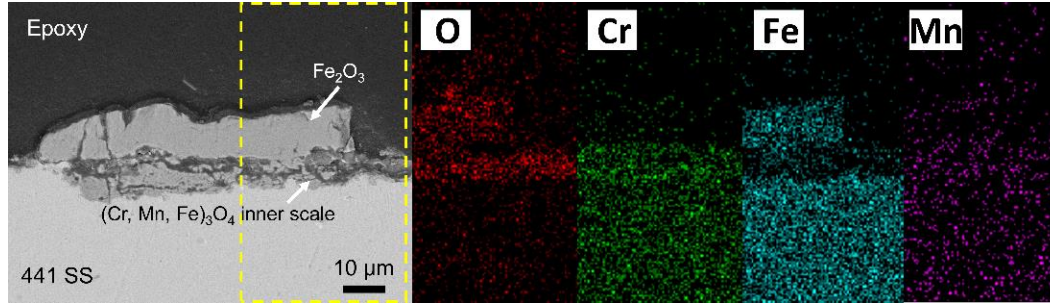
Figure 4. Oxide scale analysis for bare metals after oxidation in 50% humidified air for 500 h. Cross-sectional SEM images of (a, d, g) 430 SS, (b, e, h) 441 SS, and (c, f, i) Crofer 22 APU at

(a-c) 650 °C, (d-f) 550 °C, and (g-i) 450 °C. EDS elemental mapping of O, Cr, Fe, and Mn in (j) 430 SS, (k) 441 SS, and (l) Crofer 22 APU after oxidation at 650 °C. (m) XRD traces of the surface of 430 SS, 441 SS, and Crofer 22 APU after oxidation at 650 °C.

3.1.3. Oxidation in a dual atmosphere condition

Oxidation behavior of stainless steel at elevated temperatures and in ambient air, e.g. SOFC cathode environment, follows parabolic rate law with relatively slow Cr_2O_3 scale formation and growth observed in the microstructure [44, 61, 64]. In contrast, anomalous oxidation behavior was observed previously for SOFC interconnects tested under a dual atmosphere effect (one side exposed to air and the other exposed to hydrogen or fuel) [38-40, 65-72]. Yang et al., Kuorokawa et al., and Li et al. observed that oxidation was more severe under a higher hydrogen concentration gradient across the metal, with formation of Fe_2O_3 and Fe-depleted layers, similar to the microstructures observed above in Section 3.1.2. They proposed that the dual atmosphere effect is due to the fast hydrogen diffusion from the fuel side to the air side, which results in higher humidity formation on the air side [65, 67, 69]. Here, we assess dual atmosphere oxidation with a hydrogen gradient across the alloy for conditions relevant to PCFC/PCEC stacks. Bare 441 SS was oxidized with dry hydrogen and wet air on opposite sides for 500 h at 650 °C. Instead of the continuous Fe_2O_3 outer scale observed in single atmosphere testing, localized nodules of Fe_2O_3, together with a Fe-depleted inner zone, was observed on the air side of the stainless steel after dual atmosphere exposure, as shown in Figs 5 and supplementary S2. Interestingly, oxidation in dual atmosphere exposure was less aggressive compared to single atmosphere oxidation, but rapid non-protective Fe_2O_3 growth was still observed.
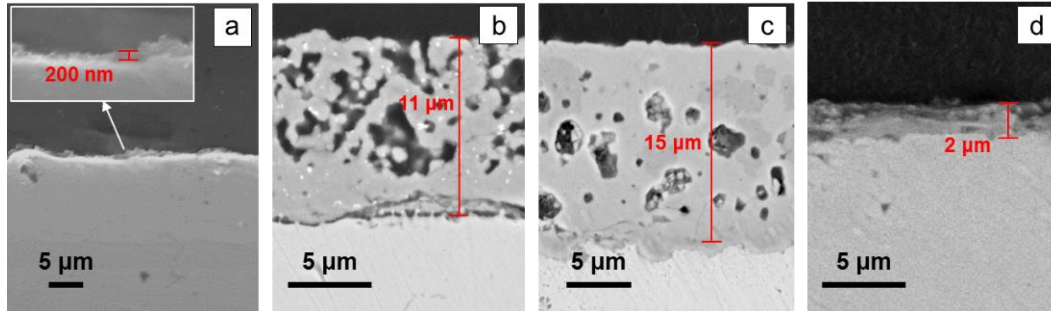
Figure 5. Dual atmosphere oxidation. SEM image and EDS elemental maps of the cross section of bare 441 SS after dual atmosphere oxidation for 500 h at 650 °C with dry hydrogen on one side and 50% steam/50% air on the other.

3.2. Oxidation of coated metals

Rapid breakaway oxidation occurs for bare ferritic stainless steels in both single and dual atmosphere conditions relevant to PCFC/PCEC interconnects, as discussed in Section 3.1 The presence of Cr vapor species evolved from the stainless steel is also known to be detrimental to PCFC electrolytes and electrodes at intermediate temperatures [20, 73, 74]. Therefore, a protective coating is deemed necessary to mitigate both Cr evaporation and corrosion of the PCFC/PCEC metallic interconnect.
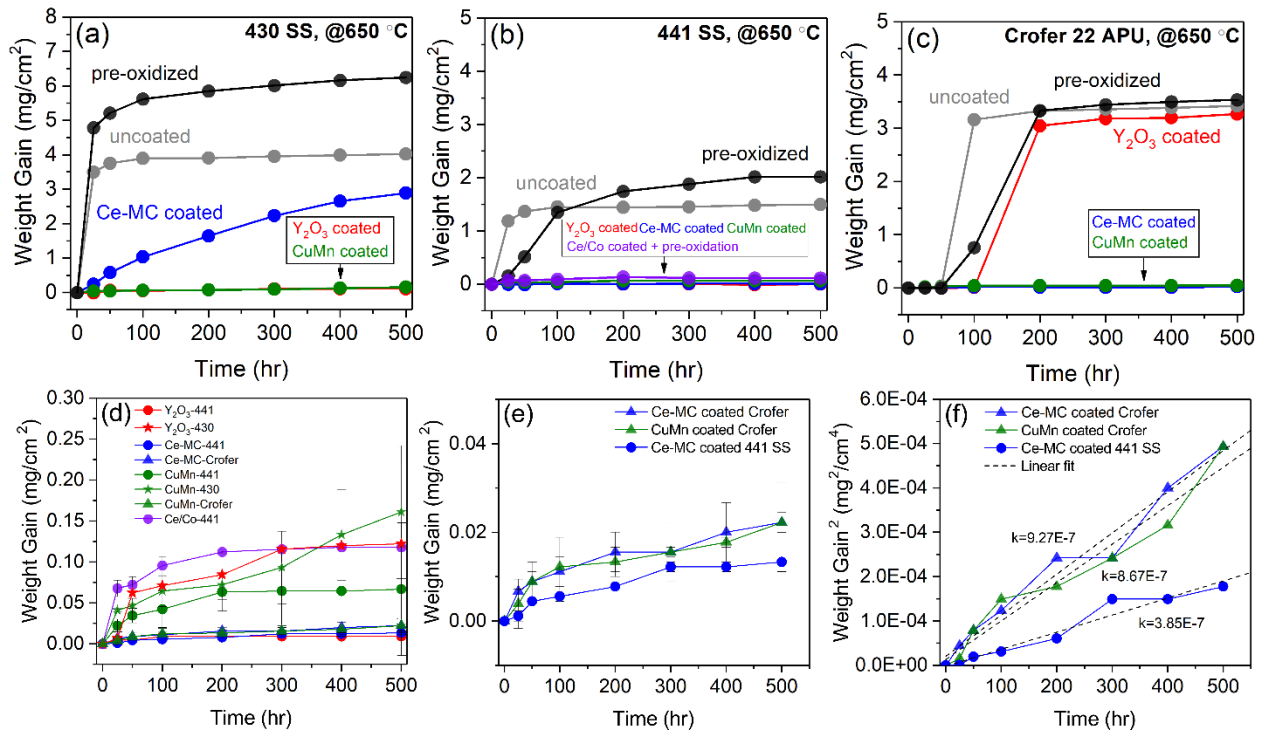
The impact of four different protective coatings, Y_2O_3, Ce-MC, CuMn, and Ce/Co, is evaluated here. The thicknesses of the Y_2O_3, Ce-MC, CuMn, and Ce/Co coatings were approximately 200 nm, 11 μm, 18 μm, and 2 μm, respectively, as seen in Fig. 6. The Y_2O_3 coating was thin with nonuniform morphology (Fig 6a). Both the Ce-MC and CuMn coatings were relatively thick and uniform, with high density at the coating-substrate interface (Fig. 6b and 6c). The CuMn coating showed a relatively denser structure than the Ce-MC coating, which was primarily due to its

higher reducing heat-treatment temperature (1000 °C for CuMn and 850 °C for Ce-MC) and longer treatment time (see Section 2.2 for details of the coating processes). Fig. 6d displays the microstructure of the Ce/Co coating after pre-oxidation at 900 °C for 10 min, showing a uniform and thin oxide layer formation on the substrate. The pre-oxidation process was conducted to convert the metallic Co to Co_3O_4 prior to oxidation testing.
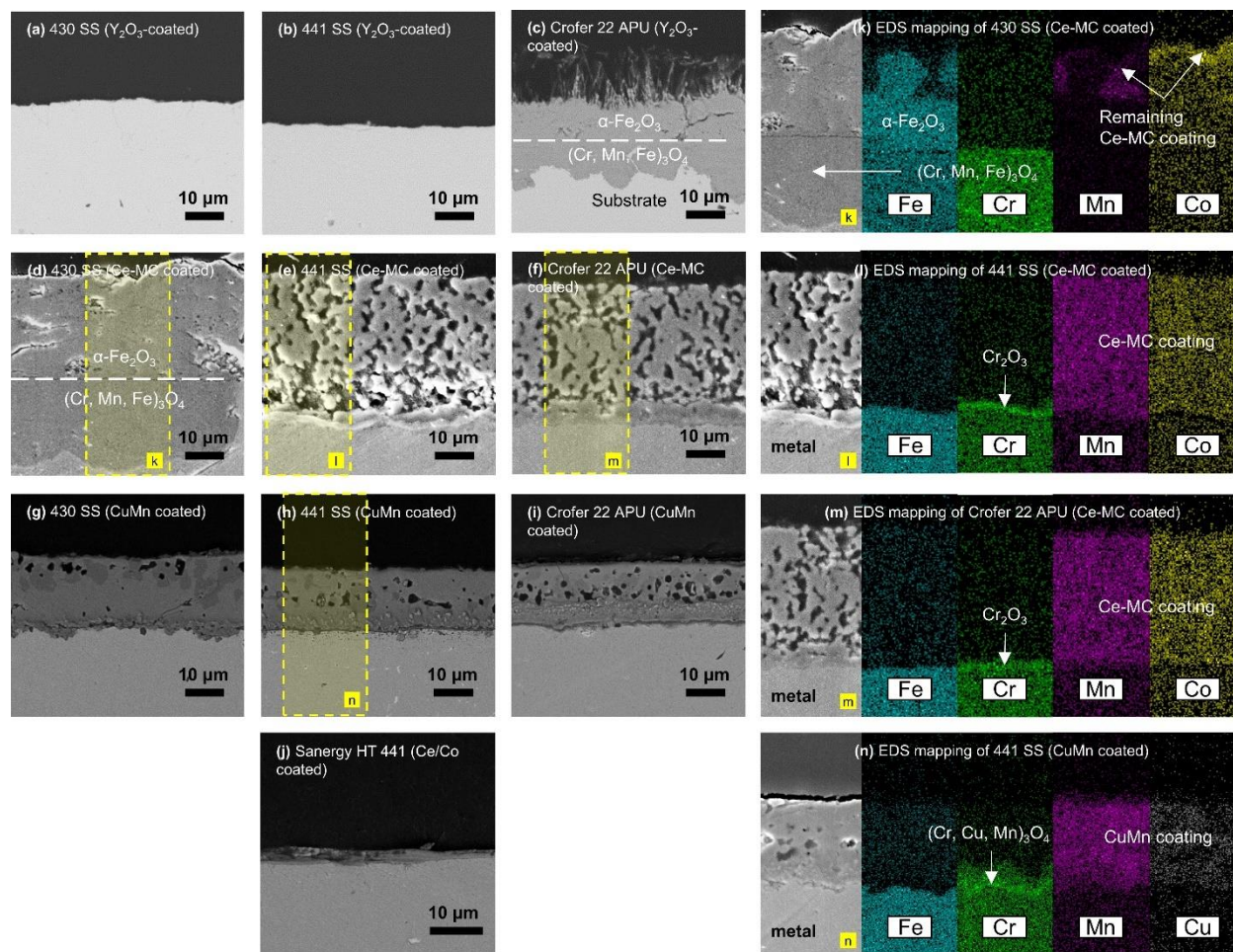

Figure 6. Cross-sectional SEM images of (a)Y_2O_3 coated metal, (b) Ce-MC coated metal, (c) CuMn coated metal, and (d) pre-oxidized Ce/Co coated metal.

Pre-oxidation is suggested in the literature as a way to improve oxidation resistance of bare alloys by forming a protective oxide scale prior to the test [41, 75]. Scale growth can also be expected to occur during the heat treatment of the coatings listed above. In order to determine the impact of pre-oxidation alone, uncoated stainless steel samples were pre-oxidized at 850 °C for 10 h. The coated, pre-oxidized, and baseline uncoated stainless steels were subjected to oxidation in 50% humidified air for a duration of 500 h at 650 °C. Table 3 lists the combinations of metal and surface modifications/coatings investigated, and summarizes the results. The weight gains of the stainless steels with different surface modifications or coatings are shown in Fig. 7, and the post-mortem microstructures of coated metals after oxidation are shown in Fig. 8.

Figure 7. Impact of coatings on oxidation. Area-specific weight gain of (a) 430 SS, (b) 441 SS, and (c) Crofer 22 APU, with different surface modifications or coatings over 500 h in 50% humidified air at 650 °C. (d) Comparison of coated metals with final weight gains less than 0.2 mg/cm^2. (e) Detailed comparison of Ce-MC- and CuMn-coated Crofer APU, and Ce-MC-coated 441 SS. (f) Parabolic rate plot with dashed lines showing the best linear fit.

Figure 8. Post-oxidation analysis of coated metals. Cross-sectional SEM images of (a) Y_2O_3 coated 430 SS, (b) Y_2O_3 coated 441 SS, (c) Y_2O_3 coated Crofer 22 APU, (d) Ce-MC coated 430 SS, (e) Ce-MC coated 441 SS, (f) Ce-MC coated Crofer 22 APU, (g) CuMn coated 430 SS, (h) CuMn coated 441 SS, (i) CuMn coated Crofer 22 APU, and (j) Ce/Co coated Sanergy HT 441, after oxidation in 50% humidified air for 500 h at 650 °C. (k-n) EDS mapping of (d, e, f, h), showing Fe_2O_3 outer scale and $(Cr, Fe)_3O_4$ or $(Cr, Mn, Fe)_3O_4$ inner scale formation under the coating.

Pre-oxidation of alloys does not prevent breakaway oxidation at 650 °C in 50% humidified air. In the case of 430 SS and 441 SS, pre-oxidation even enhanced breakaway oxidation. The formation of Cr_2O_3 or $(Cr, Mn)_3O_4$ spinel alone is clearly not sufficient to protect the substrate in the highly humidified environment.

Y_2O_3 effectively prevented breakaway oxidation of 430 SS and 441 SS, or delayed it to beyond the timescale studied here, Figs. 7a,b. After oxidation, the surfaces of 430 SS and 441 SS samples are clean, and it appears that Y_2O_3 diffused into the substrates as a well-defined coating layer is no longer present, Figs 8a,b. Breakaway oxidation of Crofer 22 APU was delayed by the Y_2O_3 coating, but similar final weight gain was obtained, Fig. 7c. In contrast to the other alloys, bi-layer oxide scales with Fe_2O_3 formation on the outside and a $(Cr, Mn, Fe)_3O_4$ spinel in the inner scale were observed, similar to uncoated Crofer 22 APU after oxidation, Figs. 4c and 8c. The reason for the failure of Y_2O_3 to protect Crofer 22 APU is unclear.

The Ce-MC coating effectively prevented breakaway oxidation of 441 SS and Crofer 22 APU, but was not protective on 430 SS. The Ce-MC coating microstructure on 441 SS and Crofer 22 APU is quite similar before and after oxidation, Figs. 6b and 8e,f. In contrast, for 430 SS, thick Fe_2O_3 outer and $(Cr, Mn, Fe)_3O_4$ inner oxide layers were formed, and the Ce-MC coating layer was consumed with only a remnant remaining at the surface of the formed Fe_2O_3 layer, Fig. 8d, k. The ineffectiveness of Ce-MC on 430 SS is speculated to result from the porosity of the coating, which allows steam to diffuse through the coating and reach the metal/coating interface, and very low tolerance of 430 SS to steam, as discussed in Section 3.1.1.

The CuMn$_{1.8}$O$_4$ coating is effective for stainless steels investigated in this study, presumably due to the relatively dense structure of the CuMn coating which effectively prevents exposure of the alloy surface to steam. The dense structure of the CuMn coating results from an EPD process where fine particles are first deposited, followed by a high temperature reduction that effectively densifies the coating layer. The CuMn coating microstructure is quite similar before and after oxidation, Figs. 6c and 8g-i, and a reaction layer containing Cr, Cu, and Mn is observed at the coating-substrate interface, Fig. 8n. This is consistent with previous observations after annealing/densification of a spinel coating due to interaction between Cr$_2$O$_3$ and the spinel oxide [28, 50, 76].

The Ce/Co coating was only available for Sanergy HT 441. After pre-oxidation at 900 °C for 10 min, the Ce/Co coating was effective in preventing breakaway oxidation, Fig. 7b. Note that the pre-oxidation step is necessary for the Ce/Co coating to be used in a humidified condition, as metallic Co has to be converted to Co$_3$O$_4$ to be protective prior to use. The Ce/Co coating microstructure is quite similar before and after oxidation, Figs. 6d and 8j.

The effectiveness of the surface modifications/coatings is summarized in Table 3. Several combinations of alloy and coating material clearly demonstrated stability in the harsh humidified air condition; these are compared in Fig. 7d. All of the coating materials, Y$_2$O$_3$, Ce-MC, CuMn, and Ce/Co, are found to be effective on 441 SS. This is not surprising, as uncoated 441 SS showed the lowest oxidation of all alloys studied (see Section 3.1.1 and Fig. 2). Oxidation data for selected combinations of alloy and coating material that show very low oxidation rate (Crofer with Ce-MC and CuMn, and 441 with Ce-MC) are compared in Fig. 7e. Weight gains of these

three coated alloys demonstrate parabolic oxidation kinetics. From the (weight gain)^2 versus time data, parabolic oxidation rate constants at 650 °C are curve-fitted to be 2.58×10^{-16}, 2.41×10^{-16}, and 1.07×10^{-16} $g^2 cm^{-4} s^{-1}$, Fig. 7f. These rates are somewhat lower than those reported previously for uncoated Crofer 22 H and Sanergy HT at 650 °C in air containing 3% H_2O (4.5×10^{-16} $g^2 cm^{-4} s^{-1}$ for both alloys) [77]. Using the obtained parabolic oxidation rate constants and assuming weight gains are due to growth of Cr_2O_3 scale without Fe breakaway oxidation, times for 3 μm scale growth (or 1.57 mg/cm^2 weight gain) for Ce-MC, CuMn coated Crofer APU, and Ce-MC coated 441 SS, are predicted to be 2654, 2839, and 6385 khr. Above about 3 μm thickness, the onset of scale spallation is expected [78]. This timescale for oxidation is much higher than the lifetime target of a PCFC stack (40-80 khr), suggesting that interconnect oxidation in the unique PCFC/PCEC environment is manageable with appropriate coatings such as those studied here.

Surface modification or coating condition	Breakaway oxidation prevented?		
	430 SS	441 SS	Crofer 22 APU
Uncoated	No	No	No
Pre-oxidized at 850 °C for 10 h	No	No	No
Y_2O_3-coated	Yes	Yes	No
Ce-MC-coated	No	Yes	Yes
CuMn-coated	Yes	Yes	Yes
Co/Ce-coated + pre-oxidized at 900 °C for 10 min	Not studied	Yes	Not studied

Table 3. Combinations of metal alloy and surface modifications/coatings investigated, and summary of oxidation behavior.

To further validate the effectiveness of the coatings, selected combinations of metals and coatings were exposed to dual atmosphere conditions at 650 °C for 500 h, including Ce-MC coated 441 SS and CuMn coated Crofer 22 APU. After dual atmosphere exposure, neither breakaway oxidation of the substrate nor structural changes of the coating materials were observed (supplementary Fig. S3).

4. Conclusions

This study demonstrated that breakaway oxidation of the metallic interconnect in PCFC/PCEC operating condition is an important oxidation mechanism that leads to rapid interconnect failure. Breakaway oxidation can be successfully mitigated by selecting effective combinations of interconnect alloy and coating material. For PCFC/PCEC stack development in the near future, this present work can be used as a guideline to identify cost-effective oxidation resistant interconnects and coating materials, as well as to determine the appropriate operating conditions to trade off stack performance and degradation.

Ferritic stainless steels, 430 SS, 441 SS, and Crofer 22 APU, were assessed to determine their viability as interconnect materials in a protonic ceramic electrochemical cell stack. The study found that the PCFC cathode or PCEC anode environment, which contains H_2O and O_2, leads to higher oxidation rates than any SOFC and SOEC environments, and therefore requires focused study. A humidified air environment was used to simulate the PCFC cathode/PCEC anode environment, and the oxidation behavior of bare metals was investigated at various intermediate temperatures (650, 550, and 450 °C). At 650 and 550 °C, breakaway oxidation was found to occur rapidly on all the studied metals, with thick Fe_2O_3 outer scales and $(Cr, Mn, Fe)_3O_4$ inner

scales observed in the microstructure after exposure for 500 h. For bare metals, the only exceptions where breakaway oxidation was not observed were 441 SS and Crofer 22 APU at 450 °C. As the performance of a PCFC/PCEC at 450 °C is relatively low, a protective coating on the metallic interconnect is deemed necessary to mitigate corrosion at higher stack operating temperature.

State-of-the-art coating materials (Y_2O_3, Ce-MC, CuMn, and Ce/Co) were applied on the stainless steels, and oxidized in humidified air conditions at 650 °C. Several combinations clearly demonstrated low oxidation rate in the harsh humidified air condition, for which the normal Cr oxidation mechanism was observed, as evidenced by parabolic oxidation kinetics. Others were found to be ineffective, and breakaway oxidation persisted. Dual atmosphere oxidation also validated the effectiveness of the selected coatings in preventing breakaway oxidation in conditions relevant to PCFC/PCEC stack operation. Future studies should include longer-term oxidation, assessment of electrical contact resistance and the impact of applied current on oxidation rate, and determining which low-cost interconnect and coating material sets should be integrated and demonstrated in a stack. The alloys and coatings studied here were adopted from the SOFC field, and therefore do not provide cost savings commonly predicted for lower-temperature operation with proton-conducting cells. Future effort may identify lower-cost coatings and alloys that are optimized specifically for the conditions of proton conducting electrolysis cell operation and maintain low oxidation rate dominated by normal parabolic Cr oxide growth.

Acknowledgements

References

[1] C. Duan, J. Tong, M. Shang, S. Nikodemski, M. Sanders, S. Ricote, A. Almansoori, R. O'Hayre, Readily processed protonic ceramic fuel cells with high performance at low temperatures, Science, 349 (2015) 1321-1326.

[2] S. Choi, C.J. Kucharczyk, Y. Liang, X. Zhang, I. Takeuchi, H.-I. Ji, S.M. Haile, Exceptional power density and stability at intermediate temperatures in protonic ceramic fuel cells, Nat. Energy 3 (2018) 202.

[3] E. Fabbri, A. D'Epifanio, E. Di Bartolomeo, S. Licoccia, E. Traversa, Tailoring the chemical stability of $Ba(Ce_{0.8-x}Zr_x)Y_{0.2}O_{3-\delta}$ protonic conductors for intermediate temperature solid oxide fuel cells (IT-SOFCs), Solid State Ionics 179 (2008) 558-564.

[4] R. Wang, C. Byrne, M.C. Tucker, Assessment of co-sintering as a fabrication approach for metal-supported proton-conducting solid oxide cells, Solid State Ionics, 332 (2019) 25-33.

[5] R. Wang, G.Y. Lau, D. Ding, T. Zhu, M.C. Tucker, Approaches for co-sintering metal-supported proton-conducting solid oxide cells with $Ba(Zr,Ce,Y,Yb)O_{3-\delta}$ electrolyte, Int. J. Hydrogen Energy 44 (2019) 13768-13776.

[6] C. Duan, R. Kee, H. Zhu, N. Sullivan, L. Zhu, L. Bian, D. Jennings, R. O'Hayre, Highly efficient reversible protonic ceramic electrochemical cells for power generation and fuel production, Nat. Energy 4 (2019) 230.

[7] Y. Chen, Y. Tang, Z. Wang, B. Zhao, Y. Wei, L. Zhang, S. Yoo, K. Pei, J.H. Kim, Y. Ding, A robust fuel cell operated on nearly dry methane at 500 °C enabled by synergistic thermal catalysis and electrocatalysis, Nat. Energy 3 (2018) 1042.

[8] L. Yang, S. Wang, K. Blinn, M. Liu, Z. Liu, Z. Cheng, M. Liu, Enhanced sulfur and coking tolerance of a mixed ion conductor for SOFCs: $BaZr_{0.1}Ce_{0.7}Y_{0.2-x}Yb_xO_{3-\delta}$, Science 326 (2009) 126-129.

[9] L. Bi, S. Boulfrad, E. Traversa, Steam electrolysis by solid oxide electrolysis cells (SOECs) with proton-conducting oxides, Chem. Soc. Rev. 43 (2014) 8255-8270.

[10] S.D. Ebbesen, S.H. Jensen, A. Hauch, M.B. Mogensen, High temperature electrolysis in alkaline cells, solid proton conducting cells, and solid oxide cells, Chem. rev. 114 (2014) 10697-10734.

[11] S. Choi, T. C. Davenport, S. M. Haile, Protonic ceramic electrochemical cells for hydrogen production and electricity generation: exceptional reversibility, stability, and demonstrated faradaic efficiency, Energy Environ. Sci. 12 (2019) 206-215.

[12] H. Iwahara, T. Esaka, H. Uchida, N. Maeda, Proton conduction in sintered oxides and its application to steam electrolysis for hydrogen production, Solid State Ionics 3 (1981) 359-363.

[13] E. Ruiz-Trejo, J. Irvine, Electrolysis of CO_2 in a proton conducting membrane, Solid State Ionics 252 (2013) 157-164.

[14] K. Xie, Y. Zhang, G. Meng, J.T. Irvine, Direct synthesis of methane from CO_2/H_2O in an oxygen-ion conducting solid oxide electrolyser, Energy Environ. Sci. 4 (2011) 2218-2222.

[15] A. Dubois, S. Ricote, R.J. Braun, Benchmarking the expected stack manufacturing cost of next generation, intermediate-temperature protonic ceramic fuel cells with solid oxide fuel cell technology, J. Power Sources 369 (2017) 65-77.

[16] C. Duan, R.J. Kee, H. Zhu, C. Karakaya, Y. Chen, S. Ricote, A. Jarry, E.J. Crumlin, D. Hook, R. Braun, Highly durable, coking and sulfur tolerant, fuel-flexible protonic ceramic fuel cells, Nature 557 (2018) 217.

[17] K. Bae, D.Y. Jang, H.J. Choi, D. Kim, J. Hong, B.-K. Kim, J.-H. Lee, J.-W. Son, J.H. Shim, Demonstrating the potential of yttrium-doped barium zirconate electrolyte for high-performance fuel cells, Nat. Commun. 8 (2017) 14553.

[18] W. Wu, H. Ding, Y. Zhang, Y. Ding, P. Katiyar, P.K. Majumdar, T. He, D. Ding, 3D Self-Architectured Steam Electrode Enabled Efficient and Durable Hydrogen Production in a Proton-Conducting Solid Oxide Electrolysis Cell at Temperatures Lower Than 600 °C, Adv. Sci. 5 (2018) 1800360.

[19] K. Leonard, Y. Okuyama, Y. Takamura, Y.-S. Lee, K. Miyazaki, M.E. Ivanova, W.A. Meulenberg, H. Matsumoto, Efficient intermediate-temperature steam electrolysis with Y:SrZrO$_3$-SrCeO$_3$ and Y:BaZrO$_3$-BaCeO$_3$ proton conducting perovskites, J. Mater. Chem. A 6 (2018) 19113-19124.

[20] H. An, H.-W. Lee, B.-K. Kim, J.-W. Son, K.J. Yoon, H. Kim, D. Shin, H.-I. Ji, J.-H. Lee, A 5×5 cm^2 protonic ceramic fuel cell with a power density of 1.3 W cm^{-2} at 600 °C, Nat. Energy 3 (2018) 870.

[21] W. Z. Zhu, S. Deevi, Development of interconnect materials for solid oxide fuel cells, Mater. Sci. Eng. A 348 (2003) 227-243.

[22] J. W. Fergus, Metallic interconnects for solid oxide fuel cells, Mater. Sci. Eng. A 397 (2005) 271-283.

[23] R. Wang, M. Würth, U.B. Pal, S. Gopalan, S.N. Basu, Roles of humidity and cathodic current in chromium poisoning of Sr-doped LaMnO$_3$-based cathodes in solid oxide fuel cells, J. Power Sources 360 (2017) 87-97.

[24] R. Wang, U.B. Pal, S. Gopalan, S.N. Basu, Chromium poisoning effects on performance of $(La,Sr)MnO_3$-based cathode in anode-supported solid oxide fuel cells, J. Electrochem. Soc. 164 (2017) F740-F747.

[25] R. Wang, Chromium poisoning of cathode in solid oxide fuel cells: mechanisms and mitigation strategies, PhD Thesis, Boston University, Boston, Massachusetts, USA, 2017.

[26] Z. Sun, S. Gopalan, U.B. Pal, S.N. Basu, $Cu_{1.3}Mn_{1.7}O_4$ spinel coatings deposited by electrophoretic deposition on Crofer 22 APU substrates for solid oxide fuel cell applications, Surf. Coat. Technol. 323 (2017) 49-57.

[27] Z. Yang, G.-G. Xia, X.-H. Li, J.W. Stevenson, $(Mn,Co)_3O_4$ spinel coatings on ferritic stainless steels for SOFC interconnect applications, Int. J. Hydrogen Energy 32 (2007) 3648-3654.

[28] R. Wang, Z. Sun, U.B. Pal, S. Gopalan, S.N. Basu, Mitigation of chromium poisoning of cathodes in solid oxide fuel cells employing $CuMn_{1.8}O_4$ spinel coating on metallic interconnect, J. Power Sources 376 (2018) 100-110.

[29] L. Blum, W.A. Meulenberg, H. Nabielek, R. Steinberger-Wilckens, Worldwide SOFC technology overview and benchmark, Int. J. Appl. Ceram. Technol. 2 (2005) 482-492.

[30] N. Sakai, H. Yokokawa, T. Horita, K. Yamaji, Lanthanum chromite-based interconnects as key materials for SOFC stack development, Int. J. Appl. Ceram. Technol. 1 (2004) 23-30.

[31] E. Dogdibegovic, R. Wang, G.Y. Lau, A. Karimaghaloo, M.H. Lee, M.C. Tucker, Progress in Durability of MS-SOFCs with Infiltrated Electrodes, J. Power Sources 437 (2019) 226935.

[32] N. Shaigan, W. Qu, D.G. Ivey, W. Chen, A review of recent progress in coatings, surface modifications and alloy developments for solid oxide fuel cell ferritic stainless steel interconnects, J. Power Sources 195 (2010) 1529-1542.

[33] J.C. Mah, A. Muchtar, M.R. Somalu, M.J. Ghazali, Metallic interconnects for solid oxide fuel cell: a review on protective coating and deposition techniques, Int. J. Hydrogen Energy 42 (2017) 9219-9229.

[34] J. Wu, X. Liu, Recent development of SOFC metallic interconnect, J. Mater. Sci. Technol. 26 (2010) 293-305.

[35] E. Dogdibegovic, R. Wang, G.Y. Lau, M. Tucker, High performance metal-supported solid oxide fuel cells with infiltrated electrodes, J. Power Sources 410 (2019) 91-98.

[36] R. Wang, E. Dogdibegovic, G.Y. Lau, M.C. Tucker, Metal-Supported Solid Oxide Electrolysis Cell (MS-SOEC) With Significantly Enhanced Catalysis, Energy Technol. 7 (2019) 1801154.

[37] A.W.B. Skilbred, R. Haugsrud, Sandvik Sanergy HT–A potential interconnect material for LaNbO$_4$-based proton ceramic fuel cells, J. Power Sources 206 (2012) 70-76.

[38] A.W.B. Skilbred, R. Haugsrud, The effect of dual atmosphere conditions on the corrosion of Sandvik Sanergy HT, Int. J. Hydrogen Energy 37 (2012) 8095-8101.

[39] P. Alnegren, M. Sattari, J.-E. Svensson, J. Froitzheim, Severe dual atmosphere effect at 600 °C for stainless steel 441, J. Power Sources 301 (2016) 170-178.

[40] P. Alnegren, M. Sattari, J.-E. Svensson, J. Froitzheim, Temperature dependence of corrosion of ferritic stainless steel in dual atmosphere at 600–800 °C, J. Power Sources 392 (2018) 129-138.

[41] C. Goebel, P. Alnegren, R. Faust, J.-E. Svensson, J. Froitzheim, The effect of pre-oxidation parameters on the corrosion behavior of AISI 441 in dual atmosphere, Int. J. Hydrogen Energy 43 (2018) 14665-14674.

[42] K. Huang, P.Y. Hou, J.B. Goodenough, Reduced area specific resistance for iron-based metallic interconnects by surface oxide coatings, Mater. Res. Bull. 36 (2001) 81-95.

[43] W. Qu, L. Jian, D.G. Ivey, J.M. Hill, Yttrium, cobalt and yttrium/cobalt oxide coatings on ferritic stainless steels for SOFC interconnects, J. Power Sources 157 (2006) 335-350.

[44] S. Fontana, R. Amendola, S. Chevalier, P. Piccardo, G. Caboche, M. Viviani, R. Molins, M. Sennour, Metallic interconnects for SOFC: Characterisation of corrosion resistance and conductivity evaluation at operating temperature of differently coated alloys, J. Power Sources 171 (2007) 652-662.

[45] S. Fontana, S. Chevalier, G. Caboche, Metallic interconnects for solid oxide fuel cell: Effect of water vapour on oxidation resistance of differently coated alloys, J. Power Sources 193 (2009) 136-145.

[46] P.Y. Hou, The reactive element effect–past, present and future, Mater. Sci. Forum 696 (2011) 39-44.

[47] Z. Yang, G. Xia, Z. Nie, J. Templeton, J.W. Stevenson, Ce-modified $(Mn,Co)_3O_4$ spinel coatings on ferritic stainless steels for SOFC interconnect applications, Electrochem. Solid-State Lett. 11 (2008) B140-B143.

[48] J.P. Choi, J.W. Stevenson, Electrically Conductive and Protective Coating for Planar SOFC Stacks, ECS Trans. 78 (2017) 1633-1640.

[49] J.P. Choi, K.S. Weil, Y.M. Chou, J.W. Stevenson, Z.G. Yang, Development of MnCoO coating with new aluminizing process for planar SOFC stacks, Int. J. Hydrogen Energy 36 (2011) 4549-4556.

[50] Z. Sun, R. Wang, A.Y. Nikiforov, S. Gopalan, U.B. Pal, S.N. Basu, $CuMn_{1.8}O_4$ protective coatings on metallic interconnects for prevention of Cr-poisoning in solid oxide fuel cells, J. Power Sources 378 (2018) 125-133.

[51] J.G. Grolig, J. Froitzheim, J.-E. Svensson, Coated stainless steel 441 as interconnect material for solid oxide fuel cells: Oxidation performance and chromium evaporation, J. Power Sources 248 (2014) 1007-1013.

[52] H. Falk-Windisch, J. Claquesin, M. Sattari, J.-E. Svensson, J. Froitzheim, Co-and Ce/Co-coated ferritic stainless steel as interconnect material for Intermediate Temperature Solid Oxide Fuel Cells, J. Power Sources 343 (2017) 1-10.

[53] Z.-Y. Chen, L.-J. Wang, F.-S. Li, K.-C. Chou, Oxidation mechanism of Fe–16Cr alloy as SOFC interconnect in dry/wet air, J. Alloys Compd. 574 (2013) 437-442.

[54] X. Cheng, Z. Jiang, B.J. Monaghan, D. Wei, R.J. Longbottom, J. Zhao, J. Peng, M. Luo, L. Ma, S. Luo, Breakaway oxidation behaviour of ferritic stainless steels at 1150 C in humid air, Corros. Sci. 108 (2016) 11-22.

[55] Z. Yang, G. Xia, P. Singh, J.W. Stevenson, Effects of water vapor on oxidation behavior of ferritic stainless steels under solid oxide fuel cell interconnect exposure conditions, Solid State Ionics 176 (2005) 1495-1503.

[56] S. Saunders, M. Monteiro, F. Rizzo, The oxidation behaviour of metals and alloys at high temperatures in atmospheres containing water vapour: A review, Prog. Mater. Sci. 53 (2008) 775-837.

[57] E. Essuman, G. Meier, J. Żurek, M. Hänsel, W. Quadakkers, The effect of water vapor on selective oxidation of Fe–Cr alloys, Oxid. Met. 69 (2008) 143-162.

[58] G. Reiss, H.L. Frandsen, Å.H. Persson, C. Weiss, W. Brandstätter, Numerical evaluation of oxide growth in metallic support microstructures of Solid Oxide Fuel Cells and its influence on mass transport, J. Power Sources 297 (2015) 388-399.

[59] J. Karczewski, T. Brylewski, T. Miruszewski, K. Andersen, P. Jasinski, S. Molin, High-temperature kinetics study of 430L steel powder oxidized in air at 600–850 °C, Corrosion Sci. 149 (2019) 100-107.

[60] T. Horita, Y. Xiong, K. Yamaji, N. Sakai, H. Yokokawa, Stability of Fe–Cr alloy interconnects under CH_4–H_2O atmosphere for SOFCs, J. Power Sources 118 (2003) 35-43.

[61] P. Jian, L. Jian, H. Bing, G. Xie, Oxidation kinetics and phase evolution of a Fe–16Cr alloy in simulated SOFC cathode atmosphere, J. Power Sources 158 (2006) 354-360.

[62] Z. Yang, M.S. Walker, P. Singh, J.W. Stevenson, T. Norby, Oxidation behavior of ferritic stainless steels under SOFC interconnect exposure conditions, J. Electrochem. Soc. 151 (2004) B669-B678.

[63] M. Palcut, L. Mikkelsen, K. Neufeld, M. Chen, R. Knibbe, P.V. Hendriksen, Corrosion stability of ferritic stainless steels for solid oxide electrolyser cell interconnects, Corros. Sci. 52 (2010) 3309-3320.

[64] S.J. Geng, J. Zhu, Z. Lu, Evaluation of Haynes 242 alloy as SOFC interconnect material, Solid State Ionics 177 (2006) 559-568.

[65] J. Li, D. Yan, Y. Gong, Y. Jiang, J. Li, J. Pu, B. Chi, L. Jian, Investigation of anomalous oxidation behavior of SUS430 alloy in solid oxide fuel cell dual atmosphere, J. Electrochem. Soc. 164 (2017) C945-C951.

[66] J. Rufner, P. Gannon, P. White, M. Deibert, S. Teintze, R. Smith, H. Chen, Oxidation behavior of stainless steel 430 and 441 at 800 C in single (air/air) and dual atmosphere (air/hydrogen) exposures, Int. J. Hydrogen Energy 33 (2008) 1392-1398.

[67] Z. Yang, G.-G. Xia, M.S. Walker, C.-M. Wang, J.W. Stevenson, P. Singh, High temperature oxidation/corrosion behavior of metals and alloys under a hydrogen gradient, Int. J. Hydrogen Energy 32 (2007) 3770-3777.

[68] Y. Zhao, J. Fergus, Oxidation of alloys 430 and 441 in SOFC dual atmospheres: effects of flow rate and humidity, J. Electrochem. Soc. 159 (2012) C109-C113.

[69] H. Kurokawa, K. Kawamura, T. Maruyama, Oxidation behavior of Fe–16Cr alloy interconnect for SOFC under hydrogen potential gradient, Solid State Ionics 168 (2004) 13-21.

[70] G.R. Holcomb, M. Ziomek-Moroz, S.D. Cramer, B.S. Covino, S.J. Bullard, Dual-environment effects on the oxidation of metallic interconnects, J. Mater. Eng. Perform. 15 (2006) 404-409.

[71] P. Gannon, R. Amendola, High-temperature, dual-atmosphere corrosion of solid-oxide fuel cell interconnects, JOM, 64 (2012) 1470-1476.

[72] M. Reisert, A. Aphale, P. Singh, Observations on Accelerated Oxidation of a Ferritic Stainless Steel Under Dual Atmosphere Exposure Conditions, in: Energy Technology 2019, Springer, 2019, pp. 273-281, https://doi.org/10.1007/978-3-030-06209-5_28.

[73] L. Zhao, D. Ding, L. Zhang, L. Gui, Z. Wang, Y. Wan, R. Wang, Y. Ling, B. He, The effect of Cr deposition and poisoning on $BaZr_{0.1}Ce_{0.7}Y_{0.2}O_{3-\delta}$ proton conducting electrolyte, Int. J. Hydrogen Energy 39 (2014) 18379-18384.

[74] Y. Hou, J. Wu, E.Y. Konysheva, Quantitative characterization of Cr-adsorption on CeO_2, pure and doped BaCeO3 and its impact on the electrochemical performance of Ce containing complex oxides, Int. J. Hydrogen Energy 41 (2016) 3994-4004.

[75] B. Talic, S. Molin, P.V. Hendriksen, H.L. Lein, Effect of pre-oxidation on the oxidation resistance of Crofer 22 APU, Corros. Sci. 138 (2018) 189-199.

[76] B. Talic, P.V. Hendriksen, K. Wiik, H.L. Lein, Diffusion couple study of the interaction between Cr_2O3 and $MnCo_2O_4$ doped with Fe and Cu, Solid State Ionics 332 (2019) 16-24.

[77] H. Falk-Windisch, J.E. Svensson, J. Froitzheim, The effect of temperature on chromium vaporization and oxide scale growth on interconnect steels for Solid Oxide Fuel Cells, J. Power Sources 287 (2015) 25-35.

[78] M.C. Tucker, Progress in metal-supported solid oxide fuel cells: A review, J. Power Sources 195 (2010) 4570-4582.